Modeling the impact of tidal flows on the biological productivity of the Alboran sea

5 AUTHORS, INCLUDING:

Cristina Naranjo
University of Malaga
15 PUBLICATIONS **51** CITATIONS

SEE PROFILE

Diego Macías
European Commission
57 PUBLICATIONS **521** CITATIONS

SEE PROFILE

J. García Lafuente
University of Malaga
114 PUBLICATIONS **1,706** CITATIONS

SEE PROFILE

Temel Oguz
Middle East Technical University
130 PUBLICATIONS **2,764** CITATIONS

SEE PROFILE

Modeling the impact of tidal flows on the biological productivity of the Alboran Sea

José C. Sánchez-Garrido[1], C. Naranjo[1], D. Macías[2], J. García-Lafuente[1], and T. Oguz[3]

[1]Physical Oceanography Group, University of Málaga, Málaga, Spain, [2]Water Research Unit, Institute for Environment and Sustainability, Joint Research Center, European Commission, Ispra, Italy, [3]Institute of Marine Sciences, Middle East Technical University, Erdemli, Turkey

Abstract The control of phytoplankton production by tidal forcing in the Alboran Sea is investigated with a high-resolution ocean circulation model coupled to an ecosystem model. The aim of the modeling efforts was to elucidate the role of tides in sustaining the high biological productivity of the Alboran Sea, as compared with the rest of the Mediterranean subbasins. It is shown that tidal forcing accounts for an increase of phytoplankton biomass and primary productivity in the basin of about 40% with respect to a nontidal circulation, and about 60% in the western Alboran Sea alone. The tidal dynamics of the Strait of Gibraltar is shown to be the primary factor in determining the enhancement of productivity, pumping nutrients from depth to the photic zone in the Alboran Sea. Model results indicate that the biological implications of the propagating internal tides are small. These results imply that nutrient transports through the Strait of Gibraltar have to be parametrized in ocean models that do not resolve tides in order to properly represent the biochemical budgets of the Alboran Sea.

1. Introduction

The Alboran Sea (AS; Figure 1a) is the first subbasin that the jet of Atlantic Water (AW) entering through the Strait of Gibraltar (SoG) encounters in its way along the Mediterranean. Its surface circulation is fairly variable in both space and time, but its most typical and classically described configuration is that consisting of the Atlantic jet meandering around and feeding two mesoscale anticyclonic gyres, the so-called Western and Eastern Alboran Gyres (hereinafter WAG and EAG). Typical velocities along the jet are as large as 1–2 m s^{-1}, and to a first approximation can be assumed to be geostrophically maintained by the strong density front between the relatively fresh incoming AW and the saltier ambient water (modified AW). As elsewhere in the ocean, such fronts feature a secondary cross-front ageostrophic circulation characterized by large vertical velocities and with potential to sustain high levels of biological productivity [e.g., *Spall*, 1995; *Nagai et al.*, 2008].

In biological terms, the AS is one of the most (if not the most) productive subbasins of the Mediterranean [e.g., *Uitz et al.*, 2012], and there are a number of physical reasons for that. The most obvious one lies in its intense frontal activity and, not surprisingly, field observations and ocean color images reveal enhanced levels of chlorophyll (chl) concentration along the jet [*Navarro et al.*, 2011]. The potential of the frontal jet ageostrophic circulation to sustain phytoplankton production has been further confirmed in the recent process-oriented model study by *Oguz et al.* [2014]. Another important factor is the wind-driven circulation, particularly that forced by westerlies that frequently drive strong upwelling events with associated phytoplankton blooms along the northern shore of the basin [*Reul et al.*, 2005; *Macías et al.*, 2007a].

There are also several short-scale processes of tidal origin occurring in the SoG that have been put forward to be relevant for the biology of the AS, although their actual impact has not been assessed yet. Of particular concern is the assumed ability of tidal flows to fertilize the surface inflowing waters through the enhancement of vertical mixing, particularly at the west side of the Camarinal Sill (CS in Figure 1b) where the flow undergoes a number of internal hydraulic transitions and high levels of turbulent energy dissipation rates have been measured during the flood tide (westward tidal flow) [*Wesson and Gregg*, 1994; *Sánchez-Garrido et al.*, 2011]. *García-Lafuente et al.* [2013] estimated that as much as 30% of the pool of mixing water formed at the lee side of the sill (west side during the flood tide), a mixture of the nutrient-impoverished AW and the nutrient-rich underlying Mediterranean Water (MW) can overpass the sill with the tidal reversal and subsequently incorporate into the
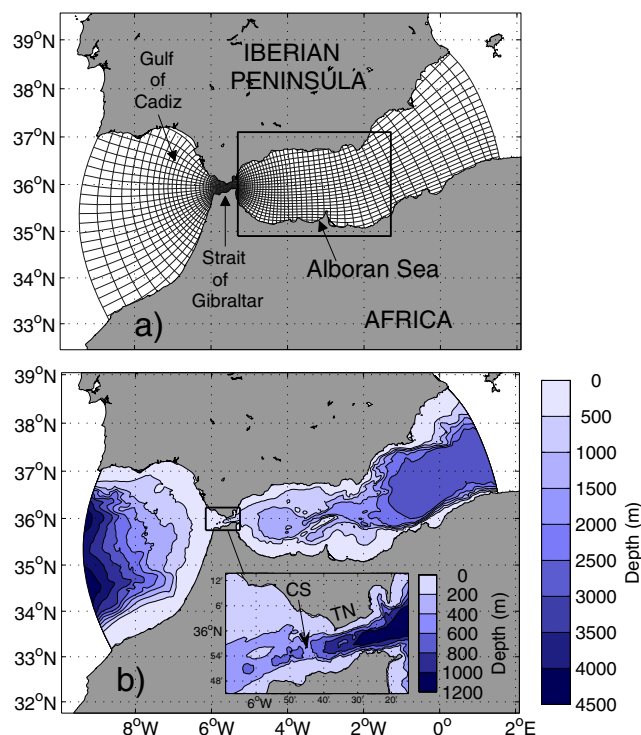
Figure 1. (a) Model domain and computational grid. For the sake of clarity, only one third of the total grid lines are shown. The rectangle encloses the Alboran Sea, the selected area in which some variables have been spatially averaged (see text for details). (b) Model bathymetry with a zoom area of the Strait of Gibraltar displayed in the inset. Two relevant bathymetric features have been labeled: Camarinal Sill (CS) and Tarifa Narrows (TN).

inflow. The likely important biological consequences of this fact was pointed out by these authors as the pool of water in question is rich in nutrients and eventually can reach the photic zone in its way to the AS, which makes it possible its utilization for photosynthesis. *Macías et al.* [2007b] drew attention to this tidal pumping of nutrients from the sill and analyzed its possible consequences for phytoplankton by applying a simple three-layer, one-dimensional (in the horizontal) model with physical domain restricted to the SoG. Despite the considerable input of nutrients, a very weak phytoplankton response was found, a fact that was attributed to the short residence time of the cells within the channel. The supply of nutrients provided by tides is therefore expected to cause certain growth of phytoplankton further downstream, somewhere in the AS, although its implications for the biology of the basin is not clear.

It is also uncertain how the prominent internal tides generated at the sill [see e.g., *Brandt et al.*, 1996; *Sánchez-Garrido et al.*, 2011] can affect productivity as they propagate in the AS. In a general context, internal waves can stimulate phytoplankton growth by enhancing vertical diffusive fluxes of nutrients from the ocean interior into the surface mixed layer, especially in shallow areas where wave-breaking occurs [*Leichter et al.*, 1998; *Sangrà et al.*, 2001]. Another way in which waves can affect production is through vertical advection, periodically exposing phytoplankton to different levels of irradiance [*Holloway and Denman*, 1989]. The potential of this mechanism was explored by *Evans et al.* [2008] in a series of field experiments conducted in a lake where photosynthesis was light limited, and reported differences of primary productivity (PP) ranging from a 15% reduction up to a 200% enhancement with respect to an unperturbed state, depending on surface irradiance. In the ocean, moderate increases of PP of $\approx$9–15%, driven by internal tides, have been reported [*Muacho et al.*, 2013; *Pan et al.*, 2012].

All these tidally driven processes were not captured by the model simulations conducted so far in the area devoted to investigate different aspects of the physical controls on PP, either by the inevitable coarse resolution applied in basin-scale models of the Mediterranean [*Lazzari et al.*, 2012], by the exclusion of tidal forcing [*Oguz et al.*, 2014], or both. The objective of the present paper is to fill this gap and clarify the role that tides play on the high productivity of the AS. For doing so, we employ a circulation model coupled to an ecosystem model that is described in the following section 2. Section 3 describes the experimental strategy that has been followed. Sections 4 and 5 present the model results and analysis, respectively, whereas discussions and conclusions are finally drawn in section 6.

2. Model Description and Initialization

2.1. Circulation Model
The physical model used in this study is the Massachusetts Institute of Technology general circulation model (MITgcm) [*Marshall et al.*, 1997a, 1997b], which solves the Boussinesq form of the Navier-Stokes

equations for an incompressible fluid on an staggered C-grid with level vertical coordinates and partial cell representation of the bottom topography. In the present work, the model utilizes the hydrostatic approximation as well as an implicit linear free surface formulation which is suitable for open ocean applications, where the free surface displacements are much smaller than the bottom depth.

The model configuration is similar as in *Sánchez-Garrido et al.* [2013]. The domain is shown in Figure 1a together with the model computational grid and bottom topography. The grid is curvilinear and has been squeezed in the AS and the SoG in order to enhance the resolution in these areas. Horizontal resolution is approximately 0.5 km within the strait, which permits a quite good representation of small-scale topographic features and processes in consideration, namely, internal hydraulic jumps with the associated mixing and propagating internal waves. In the AS (specifically within the rectangle of Figure 1a), cell sizes always lie between 1 and 4 km. Provided that the first baroclinic Rossby radius of deformation is approximately 20 km, the model is set to resolve an important wave number range of its submesoscale dynamic. In the vertical, there are 46 z-levels with increasing cell size from the surface to the bottom.

Following previous model investigations of the flow through the SoG [*Vlasenko et al.*, 2009; *Sánchez-Garrido et al.*, 2013; *Sannino et al.*, 2014], the Richardson-number-dependent scheme of *Pacanowski and Philander* [1981] is chosen for the parametrization of subgrid-scale vertical mixing:

$$v_z = v_b + \frac{v_0}{(1+\alpha \mathrm{Ri})^n}, \quad \kappa_z = \kappa_b + \frac{v_z}{(1+\alpha \mathrm{Ri})}.$$

Here v_z and κ_z are vertical eddy viscosity and diffusivity coefficients, $v_b = \kappa_b = 10^{-5}$ m^2 s^{-1} are their background values, and $v_0 = 1.5 \cdot 10^{-2}$ m^2 s^{-1}, $\alpha = 5$, and $n = 1$ are adjustable parameters. For the horizontal viscosity, the model incorporates the biharmonic Smagorinsky-like closure scheme of *Griffies and Hallberg* [2000] with free parameter $C = 3$. Temperature, salinity, and the biochemical tracers described later are advected with a third-order direct-space-time scheme with flux limiting to prevent negative values in the solutions [*Hundsdorfer and Trompert*, 1994]. The scheme is stable and sufficiently diffusive without explicit horizontal diffusion. The integration time step is 12 s.

The model is laterally forced by daily temperature, salinity, and velocity fields extracted from the Iberia-Biscay-Ireland Regional Seas reanalysis product of CMEMS (http://marine.copernicus.eu/) [*Sotillo et al.*, 2015]. Initial conditions are obtained from the same data source. At the surface the model is driven by wind stress obtained from advanced scatterometer data (ASCAT), heat fluxes, and freshwater flux originating from precipitation, both obtained from NCEP/NCAR reanalysis [*Kalnay et al.*, 1996]. Downward short wave and long wave radiation are directly prescribed, whereas sensitive and latent heat fluxes are interactively calculated by the model using standard bulk formulas. The above atmospheric forcing fields are different to those used in *Sánchez-Garrido et al.* [2013] (of less resolution), although likewise they lead to satisfactory results with maximum sea surface temperature biases of the order of 1°C. Tidal forcing has been incorporated by prescribing time-dependent barotropic velocities across the open boundaries associated with the main eight tidal constituents. Nonslip conditions are applied at the solid boundaries together with a nonlinear bottom drag at the seafloor.

The described model setup produces a realistic dynamics and circulation of the SoG and the AS that have been validated using different data sources, including ADCP measurements collected in different locations of the SoG, a number of tide-gauge records, and sea surface temperature images. For the validation analysis, the reader is referred to the papers by *Sánchez-Garrido et al.* [2013, 2014] and *Sammartino et al.* [2014].

2.2. Ecosystem Model

We considered the ecosystem model of *Follows et al.* [2007] coupled to the circulation model. The ecosystem model is of high complexity and was originally conceived to investigate the self-organization of stochastically generated phytoplankton communities. Our aim here is much simpler and a simplified configuration of the model was therefore adopted. The phytoplankton community consisted of two phytoplankton functional types: a small organism adapted to oligotrophic waters, where regenerated ammonium is the principal form of dissolved inorganic nutrient, and a big phytoplankton better adapted to nutrient-rich waters and responsible for most sinking of organic matter. The first phytoplankton type is representative of the small cyanobacteria that are dominant within the oligotrophic gyres of the AS, whereas the second type represents large eukaryotic phytoplankton that are dominant in the vicinity of the density fronts

and in coastal upwelling regions of the basin [*Arin et al.*, 2002; *Mercado et al.*, 2005]. The model also incorporates a small and a large zooplankton that preferentially graze on the small and the large phytoplankton, respectively. Provided that our aim was not at investigating biodiversity, no more complexity was added to the model. Phosphate and the inorganic forms of nitrogen (nitrate, nitrite, and ammonium) are the nutrients of the system, which can be both limiting in the AS according to the literature [*Ramírez et al.*, 2005].

The model solves a system of partial differential equations determining the evolution of dissolved nutrients, phytoplankton, zooplankton, and detritus (particle and dissolved organic matters). The governing equation for any biochemical tracer B can be written as

$$\frac{\partial B}{\partial t} = -\mathbf{u} \cdot \nabla B + \nabla \cdot (\mathbf{k}\nabla B) - \frac{\partial(w^B B)}{\partial z} + R. \tag{1}$$

The local tendency of B is then the result of advection and diffusion determined by the circulation model ($\mathbf{u}$ is the flow velocity and $\mathbf{k}$ the eddy diffusivity coefficient), sinking of the tracer (at velocity w^B), and biochemical reactions denoted by R. For instance, for phytoplankton the term R includes mortality due to grazing by zooplankton, intrinsic mortality, and a growth term depending upon environmental conditions (light, nutrients availability, and seawater temperature). Details regarding the parameterization of the biochemical reactions and parameter values for the experiments in this work are given in Appendix A; for an exhaustive description of the model, the reader is referred to *Follows et al.* [2007] and *Dutkiewicz et al.* [2009].

For the initialization of the ecosystem model, the same strategy as in *Losch et al.* [2014] has been followed. Initial and open boundary values for the tracers are prescribed distinctively depending upon the available information. For those for which there are enough observations to estimate a quasi-synoptic field, initial and boundary values have been readily derived. Nutrients are inside this category and they have been retrieved from the MEDAR/MEDATLAS database [*Maillard*, 2002]. The rest of the variables, of which we have scarce information, are initialized from few observed vertical profiles or assumed small constant concentration. For this second class of variables, we apply homogeneous Neumann boundary conditions (zero cross-boundary gradient; sensitivity runs show that this condition for the unknown tracers improves the model performance in the vicinity of the boundaries with respect to the Dirichlet condition, which requires a guessed boundary value).

Before presenting the model results, two remarks are worth noting. First, the model uses phosphorous as currency for phytoplankton growth and biomass, although we have preferred to use carbon instead throughout the paper for conventionality. The conversion has been made with the Redfield ratio C : N : P = 106 : 16 : 1. Additionally, and for validation proposes, satellite chlorophyll (chl) data have been used as a proxy of the surface phytoplankton biomass. To facilitate model-data comparisons, the model phytoplankton biomass has been converted to chl concentration by applying a constant chl : C ratio of 1 : 50, in the range of the measured quantities in the zone [*Echevarría et al.*, 2009]. Note, however, that this ratio can actually vary substantially among species and is affected nonlinearly by ambient nutrient, light, and temperatures [see e.g., *Geider et al.*, 1997]. A perfect matching between model and remote sensing observations is not to be expected then, although general spatial patterns should be similar.

3. Experimental Procedure

In a first experiment, the model is run for 3 years without tidal forcing and with the rest of the forcing fields corresponding to the period 2011–2013. The first year of simulation (2011) is taken as spin-up time and is therefore excluded from the analysis. The aim of this run is to provide a basic circulation and ecosystem state on which later to investigate the role of tides on the ecosystem. It will be referred as the reference experiment (REF). In a second run, the model includes tides (TID experiment) and their biological implications are evaluated. This run covers only 2.5 months, a subperiod of the REF run. The reason to conduct a shorter run is largely motivated by the fact that tidal forcing makes the model substantially more expensive in computational terms. On the other hand, a period of 2.5 months that encompasses several spring-neap tidal cycles (this cycle is the main source of subtidal variability) is sufficiently long to get an insight on the actual impact of tides on the biology of the AS.
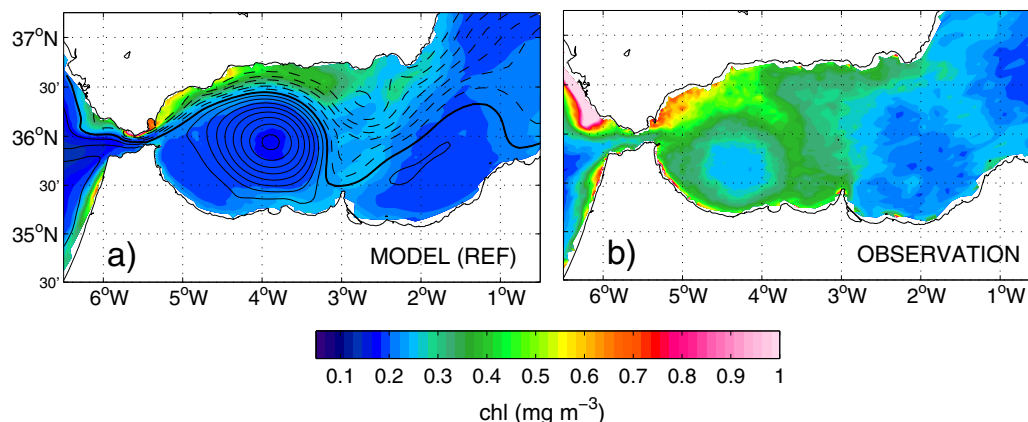
Figure 2. (a) Model-derived climatology of surface chl for the period 2012–2013 (REF experiment; median values). Black contours display the model mean SSH. The contour interval is 1.5 cm, with solid and dashed lines corresponding to positive and negative values, respectively. The thick solid line corresponds to SSH = 0. (b) Surface chl climatology derived from remote sensing images corresponding to the period 2012–2013 (median values are shown). In the computation of the climatologies, satellite data were interpolated onto the model grid and its cloud mask was applied to the model outputs for a better comparison of the two data sets.

4. Results

4.1. REF Experiment

The results of the REF run are examined in order to assess the ability of the model to reproduce the general circulation and basic biological patterns of the AS. Regional models that do not incorporate tides nor explicitly resolve the exchange flow through the SoG are successful in capturing such basic features [e.g., *Lazzari et al.*, 2012], thus great discrepancies between model and observations are not expected.

The mean sea surface height (SSH) of the simulation (black contours in Figure 2a) reveals the presence of both gyres, the WAG and EAG. The WAG has larger size and features greater geostrophic currents than its eastern counterpart, as noted by the sharper cross-gyre SSH gradients. This result stems partially from the fact that the WAG is a rather permanent feature during the simulation, while the EAG exhibits more variability in both size and location (sometimes it is even absent). Figure 2a also displays the 2 year climatology of the surface chl and reflects the oligotrophic nature of the gyres. As expected chl concentration is high in the vicinity of the jet that runs eastward with its axis centered along the SSH = 0 contour (thick solid line). This is particularly true for the cyclonic side of the frontal jet (to the north of the AS), a pattern that is consistent with a cross-front ageostrophic circulation causing downwelling at the anticyclonic side of the front, and upwelling in its cyclonic side. This creates an overall meridional gradient of chl with increasing concentration to the north of the basin. Additionally, there is a decrease of chl from west to east with the richest area being the northwestern region of the AS (NWAS), in agreement with field and remote sensing observations [see e.g., *Sarhan et al.*, 2000; *Reul et al.*, 2005; *Macías et al.*, 2007a]. *Oguz et al.* [2014] attribute the eastward decreasing pattern of chl to the gradual weakening of the density front, and thereby of its potential to fuel phytoplankton production, by accumulative mixing between incoming and ambient waters.

The spatial pattern of the surface chl in the REF run has been compared with remotely sensed chl obtained from the GlobColour Project (http://www.globcolour.info/) [*Morel et al.*, 2007]. They produce ocean color maps (Level-3) by merging data from the sensors SeaWiFS, MODIS, and MERIS. The obtained chl is for case 1 waters where phytoplankton concentration prevails over inorganic particles and the applied algorithm is based on weighted averaging merging techniques. The spatial resolution of the downloaded composite images is $1/48°$ which consist of 8 day merged fields. The climatology computed during the analyzed period (Figure 2b) displays the main features reproduced by the REF run, including the oligotrophic gyres and the biomass-rich NWAS, although with somewhat different characteristics. For instance, the chl-rich region of the NWAS is larger than in the model. Moreover, chl concentration in the WAG is considerably higher than in the EAG, both in its core and specially at the outer edges, and the west-to-east decreasing pattern of chl appears more marked than in the model. Another noticeable difference is observed over the
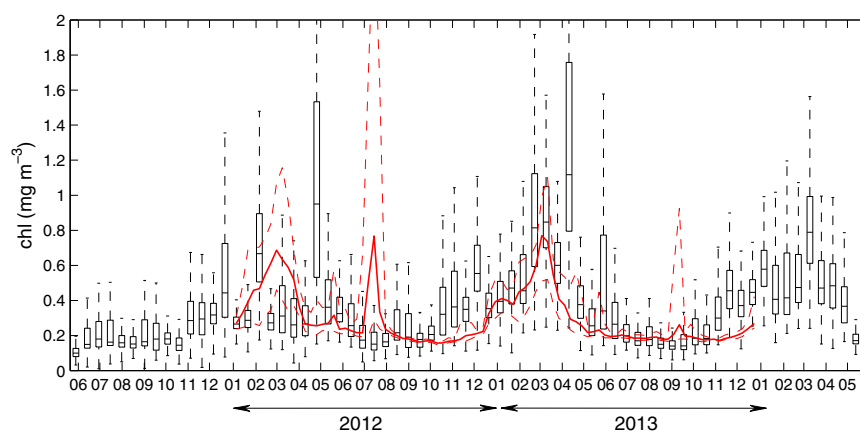
Figure 3. (a) Surface chl time variability as simulated in REF. The solid red line shows the median chl value in the basin while the dashed lines are the first and third quartiles. The box-plot corresponds to satellite data described in the text. For the computation, the model outputs have been interpolated onto the regular satellite grid and the corresponding cloud mask has been applied in order to make the two data sets comparable.

continental shelf to the north west of the SoG, where the satellite image shows the greatest chl concentration of the domain (more than 1 mg m^{-3}), whereas in the model this area is not particularly rich. These discrepancies are to a great extent due to tides, as we shall see later.

The time variability of the model and satellite chl has been also compared by computing spatial aggregate median values in the basin (Figure 3). For the computation, the model outputs were interpolated onto the satellite data grid and the cloud cover mask was applied to the interpolated chl for a more reliable comparison of the two data sets. Satellite chl (box-plot) exhibits a seasonal cycle with minimum values of chl by midsummer and maximum by the beginning of March and reflects the two regimes identified by *García-Gorriz and Carr* [1999], with a fall-to-spring bloom (November–March) and a nonbloom period (May–September). The model (red line) captures the timing and the duration of these regimes, the agreement being better in year 2013. Less satisfactory is the agreement between the timing of wind-driven bloom events due to westerlies that induce coastal upwelling along the north coast of the AS. An example is the bloom occurring in the model by July 2012 (see zonal wind stress in Figure 4b) that is not reflected in the observations. Conversely, there are some events of remarkably high chl concentration in the satellite records that are not captured by the model and could be associated with coastal upwelling as well, like the chl peak observed by the end of May 2013. There is then a mismatch in the timing of these blooms that could be ascribed to the coarse resolution of the forcing winds. Nonetheless, this is not of particular concern for the results discussed in this paper that focus on tidal processes.

Another noteworthy characteristic of the AS (and also of the rest of the Mediterranean) is the presence of a permanent deep chl maximum (DCM) with the possible exception of the late winter [*Siokou-Frangou et al.*, 2010]. Its mean depth is about 30 m and it is shallower than in the rest of the Mediterranean, presumably because of the higher productivity and hence lower seawater transparency of the AS. In the model, the maximum concentration of phytoplankton biomass is found at $z=-34\pm25$ m (Figure 4a), it deepens during summer, and shoals toward the late winter, which is in agreement with the mentioned behavior of the DCM. The most dramatic vertical excursions of the DCM take place, however, during the mentioned upwelling events when, regardless of the season the chl maximum reaches the very surface. According to the model, this occurs by mid-July 2012 and early September 2013 (Figure 4a).

The last variable examined has been the depth-integrated (net) PP (PP$_{int}$). In situ measurements reflect the great variability of the AS in both space and time with estimated PP$_{int}$ ranging in a broad interval, typically between 100 and 300 g C m^{-2} yr^{-1} [see *Siokou-Frangou et al.*, 2010, and the references therein]. Such variability has been largely attributed to the presence of the frontal jet in which a PP$_{int}$ of up to 475 g C m^{-2} yr^{-1} has been reported (1300 mg C m^{-2} d^{-1}) [*Lohrenz et al.*, 1988]. The basin-averaged PP$_{int}$ in the REF run (136.1 $\pm$ 24.6 g C m^{-2} yr^{-1}) is in the lower range of the reported values, and, as the DCM exhibits both seasonal and wind-driven variability (Figure 4b).
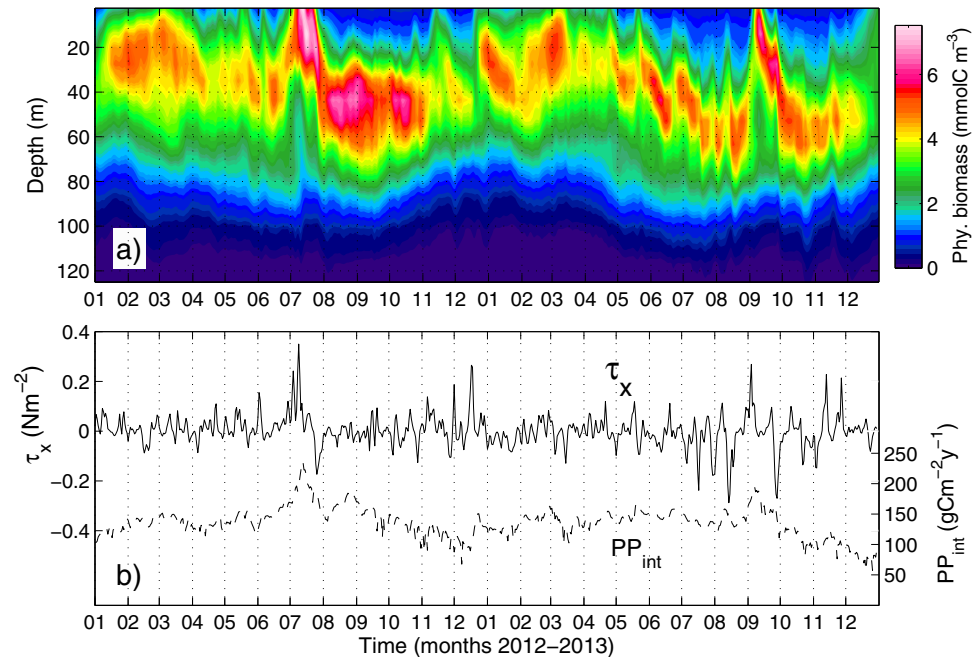
Figure 4. (a) Time-depth diagram of phytoplankton biomass horizontally averaged in the Alboran Sea (REF run; see specific domain in Figure 1). (b) Spatial mean of the zonal component of wind stress (solid line; left axis) and depth-integrated primary productivity (dashed line; right axis).
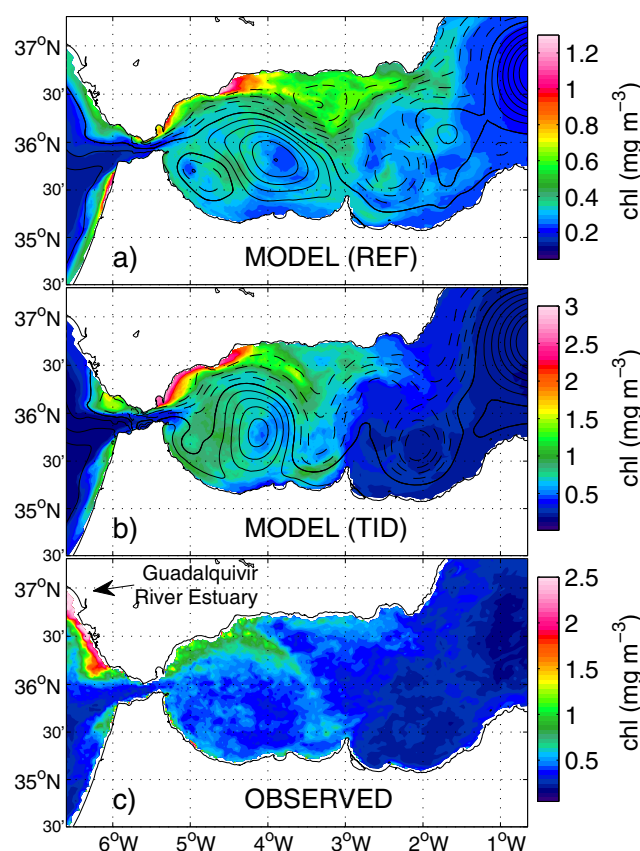
4.2. TID Experiment

In the TID experiment, the model was integrated with tidal forcing from February to June 2013 and starting from REF outputs as initial conditions. Approximately, after 1 month of simulation, the differences between the biochemical variables diagnosed in the REF and TID runs, including PP, remained stable over time, indicating that the ecosystem adjusted to the new hydrodynamic conditions after that period. The first 45 days of model outputs were then ruled out and so the final TID data set covered the last 2.5 months of the experiment (from mid-March to the beginning of June).
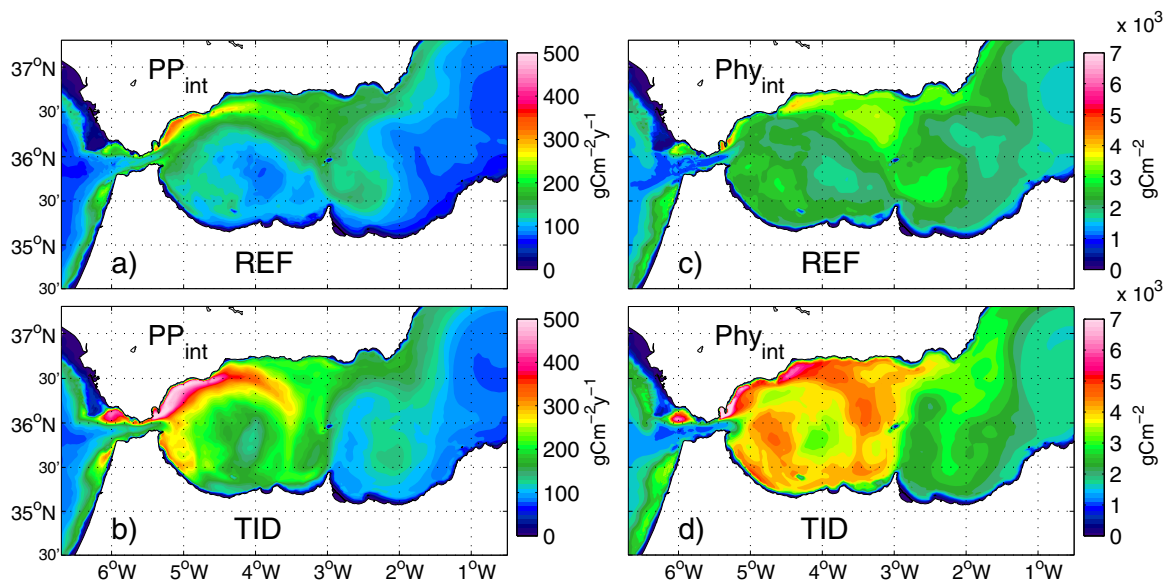
Figure 5. Mean depth-integrated primary productivity obtained in the (a) REF and (b) TID simulations (period 15 March 2013 to 1 June 2013). (c, d) Depth-integrated phytoplankton biomass. The integration interval is in both cases from the sea surface to the bottom.

Figure 6. Median surface chl obtained in the (a) REF and (b) TID experiments for the overlapping period 15 March 2013 to 1 June 2013. Black contours display the model mean SSH (contour interval is 2 cm and solid and dashed lines correspond to positive and negative values, respectively; thick solid line is SSH = 0). (c) Chl derived from satellite data for the same period. The maps are presented to illustrate the marked difference in biomass content between (c) the western and eastern half of the AS, which is well reproduced by (b) the TID run, but not by (a) the REF run. Notice the different color scales, particularly the scale of Figure 6a.

It was found that tides increased the productivity of the AS by about 40%, from a mean value of 126.6 g C m^{-2} yr^{-1} in REF to 176.7 g C m^{-2} yr^{-1} in TID (Figures 5a and 5b), this later value more in the range of reported estimates. The increase was not uniform over the basin, the ecosystem of its western half being particularly affected by tides. In the area between the SoG and 3°W, encompassing the NWAS and the WAG, the PP increment with respect to REF was 60% (from 141.4 g C m^{-2} yr^{-1} in REF to 226.1 g C m^{-2} yr^{-1} in TID), whereas in the eastern AS (east of 3°W), it was only 11% (from 111.1 to 124.1 g C m^{-2} yr^{-1}). Zones that become particularly productive with tides are the NWAS, where PP$_{int}$ locally exceeds 500 g C m^{-2} yr^{-1}, and also a small area of the continental shelf northwest of the Strait in which productivity is largely tidally driven (more than twice the REF value). This finding is in agreement with several studies that report the occurrence of intense tidal mixing in this coastal region, leading to a permanent pool of cool and nutrient-rich waters [*Vargas-Yáñez et al.*, 2002; *Ruíz and Navarro*, 2006]. Overall, phytoplankton biomass increases approximately in the same proportion as PP (Figures 5c and 5d).

Regarding the spatial pattern of chl displayed in satellite images, the inclusion of tides in the TID run results in a spatial distribution that agrees with observations much better than the REF run. Of particular concern is the much enhanced zonal chl gradient reproduced by the TID run (Figure 6b), which matches much better the west-to-east decreasing pattern of remote sensing images than the REF run (Figures 6c and 6a, respectively; note that a different color scale has been chosen in these panels with the aim to highlight surface chl patterns). The TID run also gives rise to a localized spot of high chl concentration in the aforementioned region of the continental shelf Northwest of the SoG (Figure 6b), although it is still unable to reproduce the high chl signal along the Spanish coast displayed in the satellite image (Figure 6c), a fact that we attribute to nutrient loads from the Guadalquivir River that were not prescribed in the model.
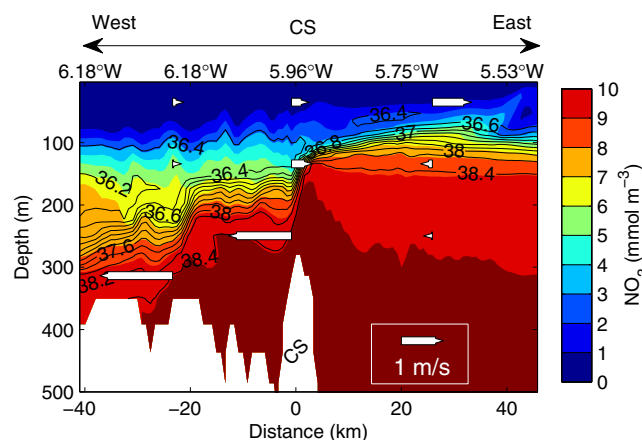
5. Analysis

Here we analyze the candidate physical processes for explaining the tidally driven increase of the AS productivity. First, we assess the hypothesis that tidal flows in the SoG fertilize the Atlantic inflow. The tidal dynamic of the strait is examined and nutrient transports into the AS will be computed for both the REF and TID simulations. Attention will be also paid to other tidal processes with possible biological consequences such as propagating internal waves.

5.1. Tidal Dynamics and Nutrient Transports Through the SoG

The configuration of the flow through the SoG as simulated in the REF run is shown in Figure 7, displaying salinity, velocity, and nutrient concentration (nitrate) along the strait. The flow consists of an undercurrent

**Figure 7.** Vertical cross section of nitrate (color contours), salinity (line contours; contour interval is 0.2), and zonal velocity (arrows) along the central axis of Strait of Gibraltar. The fields correspond to a snapshot of the REF experiment. The bottom x axis indicates distance from the Camarinal Sill (CS), with positive (negative) values toward the east (west) of the sill. The top x axis indicates longitude.

of nutrient-rich and salty MW (>8 mmol NO_3 m^{-3}; $S > 37$) flowing westward, and AW flowing to the AS ($S < 37$), which can be further partitioned into the nutrient-depleted Surface Atlantic Water (SAW; <3 mmol NO_3 m^{-3}) and the moderately nutrient-rich North Atlantic Central Water (NACW; ≈5–7 mmol NO_3 m^{-3}). The NACW is fresher but denser than the overlying SAW lies to the west of the Camarinal Sill at 150–200 m depth, with a salinity of S ≈ 36.2–36.4. With this configuration, the nutrient budget of the inflow is largely dependent upon the volume of NACW that can overpass the sill and participate in the inflow, as well as on the ability of the Atlantic current to entrain nutrients from the underlying MW. Figure 7 suggests that the second mechanism is at work 30 km to the east of the sill, in the so-called Tarifa Narrows (TN in inset of Figure 1b), where the inflow accelerates in response to the constricted lateral boundaries.

The steady exchange in the REF run is notably modified in the TID run as it can be seen in the time evolution of the flow during a tidal cycle presented in Figure 8. Figure 8a roughly corresponds to the time of maximum tidal flow toward the Atlantic (flood tide; see barotropic velocity over the sill in the bottom figure)
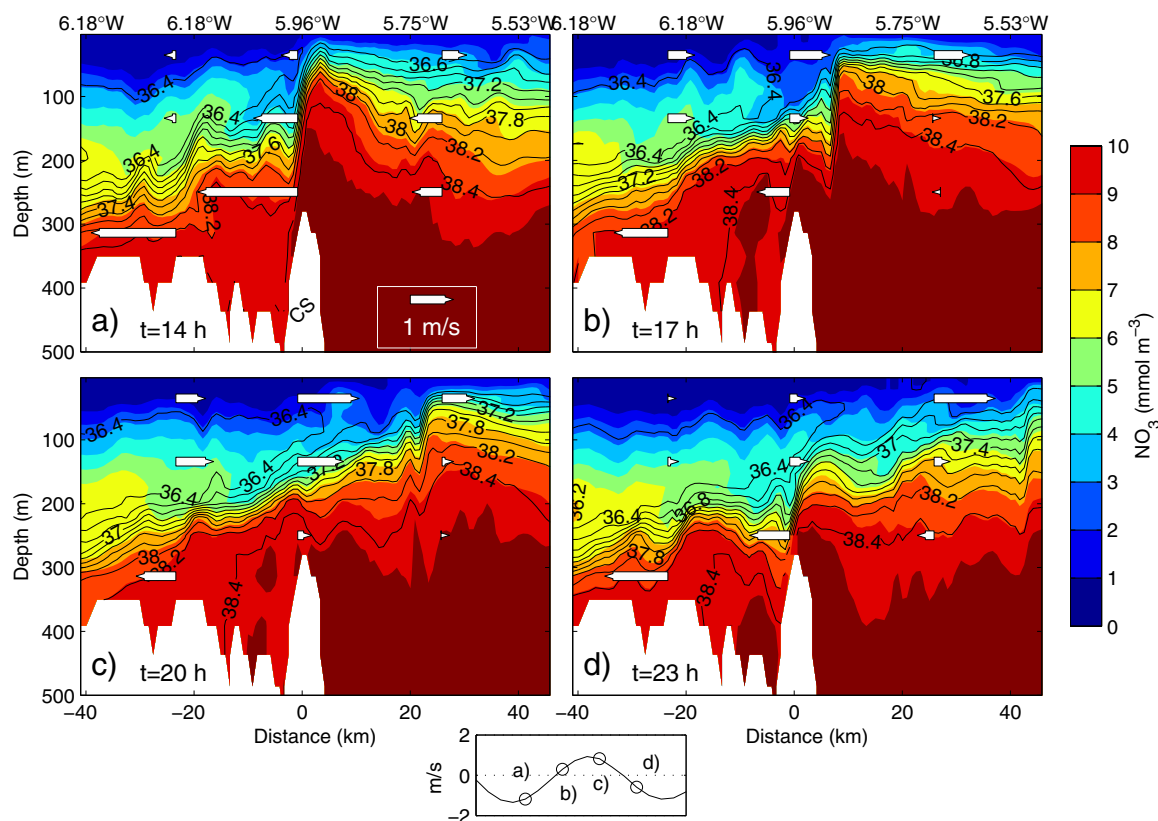
Figure 8. Same as Figure 7 for a tidal cycle of the TID simulation. Time increases from Figures 8a–8d with a time interval of 3 h. Time is given in hours from 15 March 2013. The bottom axis displays the barotropic (depth-average) velocity over the Camarinal Sill.
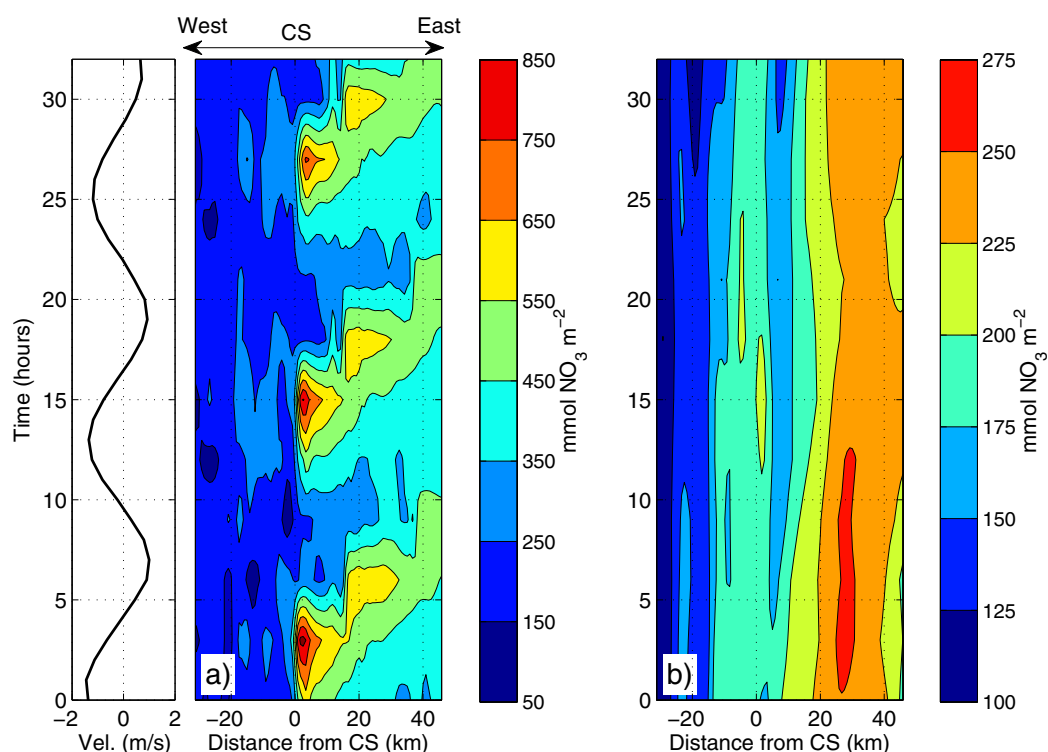
Figure 9. Temporal and spatial dependence of the depth-integrated nitrate along the central axis of the Strait of Gibraltar. Nitrate concentration is integrated from $z = -94$ to $z = 0$, $\int_{-94}^{0} NO_3 \, dz$. (a) Corresponds to the TID run, with the leftmost axis showing the barotropic (depth-average) velocity over the Camarinal Sill, while (b) corresponds to the REF run. Time is given in hours from 15 March 2013.

and reflects important differences with respect to the steady flow configuration described above. The response of the flow to the tidal discharge is the expected for a hydraulically controlled sill flow exposed to a quasi-steady barotropic forcing [*Long*, 1954; *Lawrence*, 1993] both upstream (to the right) and downstream (left) of the bottom obstacle (the terms upstream/downstream are with respect to the barotropic flow). In the upstream side, the flow adjusts to the tidal forcing by raising the interface between Atlantic and Mediterranean Waters, in a clear manifestation of upstream influence exerted by the sill, whereas the most noticeable downstream effect is the enhancement of vertical mixing, as noted by the homogenization of both salinity and nutrient concentration over the water column. Such enhanced of mixing is closely related to the increase of the internal Froude number at the downstream side of the sill [*Sánchez-Garrido et al.*, 2011].

The biological implications of the tides are revealed in the subsequent stages of the tidal cycle, when the tidal flow turns to the east (ebb tide; Figures 8b and 8c). Tidal forcing is sufficiently strong to invert the direction of the Mediterranean current over the sill, temporally facilitating the eastward advection of both NACW and MW, the later returning to the eastern flank of the sill with the tidal reversal (note positive velocities all over the sill crest in Figure 8c). In fact, *García-Lafuente et al*. [2013] estimate that as much as 30% of the pool of mixed water formed west of the sill during the flood tide, a mixture of NACW and MW, can be subsequently pumped to the near surface in the eastern part of the strait, providing a nutrient supply to the AS. A second way in which tides can fertilize the inflowing waters is through the enhancement of diapycnal mixing to the east of the sill, driven in part by the eastward propagation of the internal tidal bore generated at the sill (note it, for instance, at $x = 22$ km in Figure 8c).

The strong time dependence of the flow is transferred to the nutrient budget of the inflowing waters, as noticed in Figure 9 that shows the time-space dependence of nitrate integrated in the uppermost 94 m of the water column. The maximum nutrient content is periodically reached in Camarinal Sill ($x = 0$) around the end of the flood tide as a result of the shoaling of the interface (see Figure 8a) and moves eastward during the ebb tide at a velocity that can be estimated in 1.5 m s^{-1} from the slope of the contours in the time-space diagram of Figure 9a. *García-Lafuente et al.* [2013] described a similar eastward propagation pattern
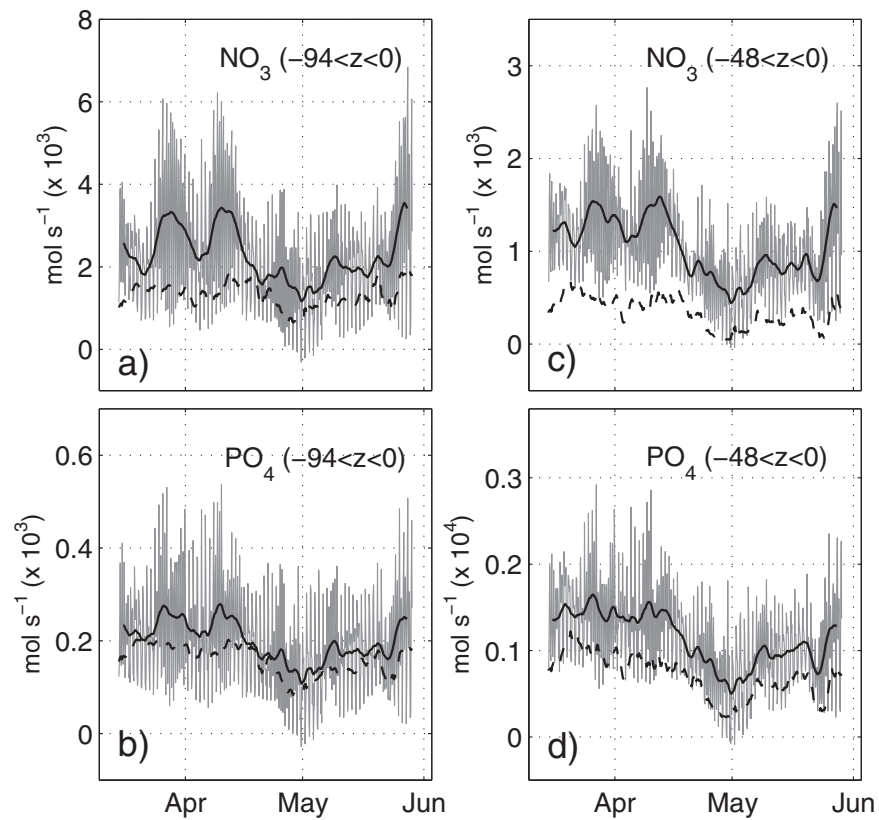
Figure 10. (a) Nitrate transport at the eastern end of the Strait of Gibraltar ($x = 40$ km in Figure 7) as simulated in the TID (gray line; 3 h data) and REF (black dashed line) runs. The black solid line if the low-pass TID series (tidal variability removed). The transport is computed in the first 94 m of the water column, roughly encompassing the inflowing Atlantic layer. (b) Same as Figure 10a but with the transport computed in the first 48 m of the water column. (c and d) Same as Figures 10a and 10b but for phosphate.

of the thickness of the interface mixing layer and ascribed it to the physical processes mentioned above, namely, advection of mixed water formed west of the sill and enhanced entrainment of MW driven by the propagating baroclinic bore. The same processes are very likely involved in the eastward propagation of nutrients from the sill with tidal modulation. This behavior differs from the REF run, in which the nutrient budget of the inflow hardly exhibits time dependence. It is from the Tarifa Narrows that it increases eastward (Figure 9b), due to the enhanced entrainment of MW driven by the spatial acceleration of the inflow in this location, as remarked earlier. Most importantly, the nutrient content of the inflow at the eastern mouth of the SoG ($x = 45$ km) is greater in the TID experiment, oscillating between 350 and 550 mmol NO_3 m^{-2}, against the more constant value of 200–250 mmol NO_3 m^{-2} obtained in REF, which results in different nutrient transports into the AS in the two model simulations (Figure 10).
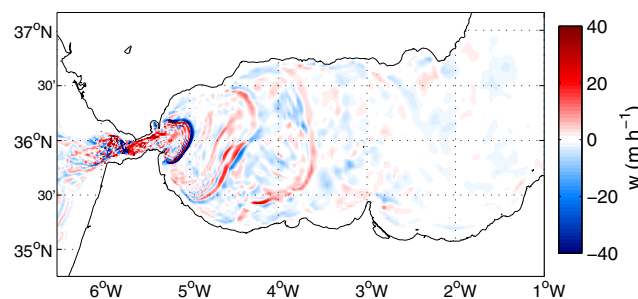
Figure 11. (a) Synoptic vertical velocity field at $z = -88.5$ m, as simulated in the TID experiment.

The nitrate transport in TID (Figure 10a; gray line) has a mean $\pm$ SD value of 2.28 ± 1.28 kmol s^{-1}, nearly 75% greater than in REF (1.31 ± 0.28 kmol s^{-1}; black dashed line). The greater variability of the TID series is largely accounted for the M_2 tidal constituent, although a noticeable fortnightly signal can be also distinguished, with greater and smaller transports during spring and neap tides, respectively, as highlighted by the low-pass curve (tidal variability
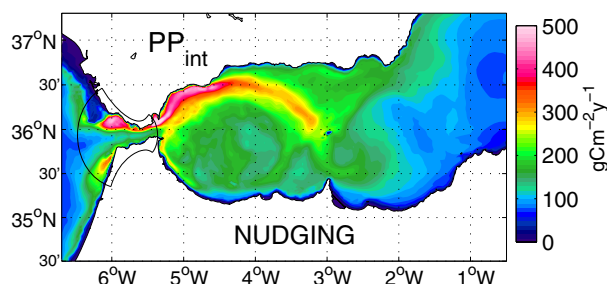
Figure 12. Mean depth-integrated primary production obtained in the nudging experiment. The polygon around the Strait of Gibraltar encloses the area where the nudging term described in the text has been applied.

filtered out; black solid line). The same applies to phosphate, although differences between the two simulations are slightly more moderate (0.20 ± 0.10 and 0.15 ± 0.03 kmol s^{-1} in TID and REF, respectively; Figure 10b). Note that these discrepancies are of particular concern because the input of nutrients provided by tides is within the photic zone and so can be utilized by phytoplankton. This becomes even more obvious by noting that the nutrients' transports in TID are even greater with respect to those in REF when computed in the upper part of the photic zone ($-48 < z < 0$; Figures 10c and 10d), where high levels of light can further stimulate phytoplankton growth. The tidal pumping of nutrients from the sill is therefore a clear candidate to explain the increase of biomass and productivity obtained in the TID simulation.

5.2. Tides and Tidal-Related Processes in the AS

It is also feasible that the different biological patterns of the TID and REF runs are accounted for, at least partially, by local tidal currents in the AS, rather than in the adjacent SoG. For instance, a distinctive feature of the tidal experiment is the internal tide that progresses eastward through the SoG into the AS after being generated in the Camarinal Sill (Figure 8). Such internal waves induce large vertical velocities (Figure 11) that can potentially modify phytoplankton growth by exposing it to different levels of irradiance through vertical advection. Another tidal-related process that bears consideration refers to lateral boundary flows. *Sánchez-Garrido et al.* [2013] found that the back and forth motion of tides generate shear vorticity on the strait's lateral boundary layers (positive on the north, negative on the south) that can lead to a wake of coherent submesoscale eddies carried by the Atlantic jet [see also *La-Violette*, 1984]. The flow along the wake is very ageostrophic and can stimulate productivity, much like observed in island wakes [*Hammer and Hauri*, 1981; *Hernández-León*, 1991; *Hasegawa et al.*, 2004].

In order to clarify whether these processes are biologically relevant, a third experiment has been conducted in which the physics is as in the REF run but with modified ecosystem equations so that biochemical tracers are nudged toward their TID values within the SoG. Specifically, a Newtonian nudging term $\tau^{-1}(B - B_{tid})$ was added to the right-hand side of equation (1), where B_{tid} denotes the value of the biochemical tracer obtained in the tidal simulation (daily mean fields) and τ is the relaxation time scale. For a sufficiently small τ, the nudging term acts more like a forcing rather than a relaxation term, forcing the tracer to lie very close to B_{tid} during the calculations. The nudging term is only included within the SoG and a small relaxation time scale is set, $\tau = 2$ h. With this constraint, nutrients concentration and the corresponding transports through the SoG in the new run are very similar to those obtained in TID, approximately following the low-pass curves of Figure 10 (not shown). Note, however, that even if the transports are maintained as in TID, the circulation is nontidal and therefore vertical fluxes driven by internal waves, eddies, or any other tidal-related process occurring in the AS are now inhibited. As such, this experimental strategy allows us to distinguish between biological effects resulting from (i) the increase of nutrient transports through the SoG and (ii) tidally driven flows in the AS itself.

The mean PP$_{int}$ obtained in the nudging experiment is shown in Figure 12. As tidal forcing is suppressed in this experiment, the surface structures (suggested by the PP$_{int}$ distribution) in the AS resemble those found in the REF run (compare Figures 5 and 12a), but the PP$_{int}$ values themselves are similar to those obtained in the TID run (Figure 5b), with PP$_{int}$ exceeding 400 g C m^{-2} yr^{-1} in the NWAS, 300–400 g C m^{-2} yr^{-1} further east along the jet, and ≈ 150 g C m^{-2} yr^{-1} in the center of the WAG. The same level of similarities is found in terms of integrated biomass (not shown). There are however some differences of PP$_{int}$ distribution between Figure 12 (Nudged run) and Figure 5b (TID run). One of them is the extent of the plume of high productivity associated with the Atlantic jet, which reaches further east in the Nudging run (Figure 12). This in turn leads to a slightly greater production in the eastern AS (compare Figures 5 and 12b). Another small difference is found at the exit of the SoG at 5°W, where the TID run produces greater values of PP$_{int}$ off the

African coast. Both differences are ascribed to the different advection/diffusion of the biochemical tracers in the TID and nudging runs. Despite these differences, the comparison of Figures 5 and 12b strongly suggests that (i) is the prevailing mechanism for the tidally driven increase of biomass and productivity.

6. Discussion and Conclusions

The results of this paper highlight the important role of tides for maintaining the high productivity of the AS, as compared with the rest of Mediterranean subbasins. The tidal dynamics of the flow through the SoG, with the resulting pumping of nutrient-rich water from depth to the sunlit surface layer is the key process that explains the increase of biomass and productivity in the tidal simulation. The nutrient supply provided by tides does not cause, however, a substantial growth of phytoplankton within the strait itself (see Figure 5d), a fact that agrees with the findings of *Macías et al.* [2007b] and that we ascribe to the short residence time of the cells within the channel. The distance from the Camarinal Sill to the eastern mouth of the SoG is 40 km and a typical along-strait velocity is 1.5 m s^{-1}, which gives a residence time of $\approx$ 7.5 h, too short indeed for a noticeable increase of biomass (phytoplankton growth rate is no greater than 2.5 day^{-1}), initially scarce at the western side of the SoG except for a limited region of its north coast. It is not until the bulk of nutrients is carried into the AS that it has an apparent impact on biochemistry, especially in the western half of the basin where it accounts for as much as a PP$_{int}$ increase of 60%. By contrast, the eastern AS is barely affected by such nutrient supply which suggests that the input of nutrients coming from the SoG is consumed by phytoplankton in the western half of the basin. This is particularly true for the region of the NWAS where the maintenance of its nutrient-rich waters and elevated biomass concentration has been so far attributed to its upwelling dynamics [*García-Gorriz and Carr*, 1999; *Sarhan et al.*, 2000].

By conducting an idealized experiment in which biochemical tracers (and associated transports) were locally restored to their tidal values within the SoG, local processes occurring in the AS have been ruled out from being responsible for the increase of biomass and productivity resulting in the tidal simulation. A prominent feature of the AS is the large internal tides that propagate in the basin, which however were found to play a negligible role on the ecosystem. While the model captures well the propagation of internal tides (of $\approx$ 50 km wavelength) in open waters and so also the associated vertical advection of biochemical tracers, smaller-scale features and processes such as short solitary waves evolving from the baroclinic bore generated in the strait's sill and their expected wave-breaking over shelf areas of the AS are not resolved in the simulation. It is then likely that internal waves can actually be more relevant over coastal regions that our model suggests.

A delicate point implicit in our results lies in the ability of the model to reproduce a realistic tidal dynamic and associated mixing in the SoG. The application of a high-resolution model configuration is necessary to achieve this but does not necessarily guarantees a satisfactory outcome. Of particular concern are the resulting nutrient transports that largely determine the biological response in the adjacent AS. The assessment of the validity of our results requires the comparison with estimates based on the scarce field observations collected in the area, like those included in the paper by *Huertas et al.* [2009]. These authors estimate a mean nitrate and phosphate transports of 2.59 and 0.21 kmol s^{-1}, respectively, which agree quite well with the values obtained in the TID simulation (2.28 and 0.20 kmol s^{-1}; see Figure 10) and exceed those of REF. Regional ocean models of the Mediterranean do not typically incorporate tidal forcing as it is generally assumed to have minor effects on the circulation and therefore also on biochemistry. This is not true for some locations and the AS is one example in light of the results presented herein. Attention needs to be paid to the transports obtained in these models as the simulated inflowing waters can be less nutrient-rich than they actually are.

The last remark concerns implications of our results for the future in which a decline of marine PP is expected for the low and midlatitude ocean, including the Mediterranean [*Steinacher et al.*, 2010]. The decline is related to enhanced stratification and reduced mixed layer depth by the end of the 21st century, which limits vertical fluxes of nutrients into the euphotic zone. In such scenarios, dynamical regions with strong energy sources such those originating from tides are expected to be less vulnerable, as it can be the case of the AS.

Appendix A: Ecosystem Model

We use a two-species configuration of the ecosystem model developed by *Follows et al.* [2007] with the modifications introduced by *Dutkiewicz et al.* [2009]. The reader is referred to these papers for an exhaustive

description of the model theoretical background, equations, and parametrizations; here we only outline the basic features and details of our setup. The two types of phytoplankton consist of a large organism with the ability to rapidly develop in situations of abundant nutrient supply, and a smaller class adapted to low-nutrient conditions. In our configuration, the inorganic forms of nitrogen and phosphorus nourish the two phytoplankton types. There is also a large and a small zooplankton that preferentially graze on the large and the small phytoplankton, respectively, although can also graze on the other. Two maximum grazing rates g_{max} are therefore defined and their given values will be specified later. Mortality of and excretion from the plankton community as well as sloppy feeding by zooplankton contribute to a sinking particulate and dissolved organic matter that eventually transform into inorganic forms by remineralization.

The local tendency for each phytoplankton depends upon advection and diffusion determined by the circulation model, grazing, intrinsic mortality rate, sinking speed, and a growth term depending upon environmental conditions. The latter is written as

$$\mu_j = \mu_{max_j} \gamma_j^T \gamma_j^I \gamma_j^N,$$

where μ_{max_j} is the maximum intrinsic growth rate and γ_j^T, γ_j^I, γ_j^N are nondimensional factors that modify μ_{max_j} due to ambient temperature, light, and nutrient availability, respectively. Subscript j refers to the phytoplankton type, with $j = 1$ for the large type and $j = 2$ for the small type. Primary productivity is $\sum_j \mu_j P_j$, where P denotes phytoplankton concentration.

The temperature modification of the growth rate is

$$\gamma_j^T = \frac{1}{\tau_1}(A^T - \tau_2),$$

where T is the local ocean temperature, coefficient A regulates the shape of the curve, and τ_1 and τ_2 normalize the maximum value of the modification function.

Light modification is parametrized as

$$\gamma_j^I = \frac{1}{F_{max}}(1 - e^{-k_{par_j}I})e^{-k_{inhib_j}I},$$

where I is the local vertical flux of photosynthetically active radiation (PAR), k_{par_j} defines the increase of growth rate with light at low levels of irradiation, and k_{inhib_j} regulates the rapidity of the decline of growth efficiency due to photoinhibition. The coefficient F_{max} is chosen as to normalize the maximum value of γ_j^I to unity, whereas the local PAR has been attenuated through the water column including the effects of shelf-shading:

$$I(z) = I_0 \cdot \exp\left[-k_w|z| - k_c \int_z^0 \sum_j P_j(z) dz\right].$$

Here I_0 is the surface PAR, k_w the attenuation coefficient for water, and k_c for phytoplankton.

Nutrient limitation is determined by the most limiting nutrient:

$$\gamma_j^N = \min(N_{PO_4}^{lim}, N_N^{lim}),$$

where N_{PO_4} and N_N denote nutrient phosphate and dissolved inorganic nitrogen. The effect of phosphate concentration on phytoplankton growth rate is represented by a Michaelis-Menten function

$$N_{PO_4}^{lim} = \frac{N_{PO_4}}{N_{PO_4} + \kappa_{PO4_j}},$$

with κ_{PO4} the half-saturation constant for phytoplankton type j with respect to the ambient concentration of phosphate. The model resolves three potential sources of inorganic nitrogen (ammonium, nitrite, and nitrate) and in our configuration phytoplankton is able to assimilate all of them. The effect of nitrogen concentration on the grow rate is modified as follows in order to reflect the inhibition of nitrate and nitrite uptake due to ammonium

$$N_N^{lim} = \frac{NO_3 + NO_2}{NO_3 + NO_2 + \kappa_{IN}} e^{-\psi NH_4} + \frac{NH_4}{NH_4 + \kappa_{NH4}}.$$

Table A1. Ecosystem Model Parameters and Given Values[a]

Parameter	Symbol	Value	Units
Maximum growth rates	μ_{max_1}, μ_{max_2}	2.5, 1.4	day^{-1}
Phytoplankton mortality rates	m_1^p, m_2^p	0.1, 0.1	day^{-1}
Phytoplankton sinking rates	w_1^p, w_2^p	0.5, 0	$m\ d^{-1}$
Phosphate half-saturation const.	$\kappa_{PO4_1}, \kappa_{PO4_2}$	$3.5 \times 10^{-2}, 1.5 \times 10^{-2}$	$\mu M\ P$
Nitrate+nitrite half-saturation const.	$\kappa_{IN_1}, \kappa_{IN_2}$	0.56, 0.24	$\mu M\ N$
Ammonium half-saturation const.	$\kappa_{NH4_1}, \kappa_{NH4_2}$	0.28, 0.12	$\mu M\ N$
Ammonium inhibition	ψ	4.6	$(\mu M\ N)^{-1}$
PAR saturation coeff.	k_{par_1}, k_{par_2}	$1.2 \times 10^{-2}, 1.2 \times 10^{-2}$	$(\mu E\ m^{-2}\ s^{-1})^{-1}$
PAR inhibition coeff.	k_{inhib_1}, k_{inhib_2}	$10^{-3}, 6 \times 10^{-3}$	$(\mu E\ m^{-2}\ s^{-1})^{-1}$
Temperature curve coeff.	A	1.04	
Temperature normalization coeff.	τ_1, τ_2	3, 0.3	
Zooplankton mortality rate	m^z	3.3×10^{-2}	day^{-1}
Maximum grazing rates	g_{max_a}, g_{max_b}	$0.2, 3.3 \times 10^{-2}$	day^{-1}
Grazing half-saturation const.	K^p	0.1	$\mu M\ P$
DOM remineralization rates	r_{DOP}, r_{DON}	$10^{-2}, 10^{-2}$	day^{-1}
POM remineralization rates	r_{POP}, r_{PON}	$2 \times 10^{-2}, 2 \times 10^{-2}$	day^{-1}
POM sinking rate	w_{POM}	10	$m\ d^{-1}$
Attenuation coefficient of water molecules	k_w	0.04	m^{-1}
Attenuation coefficient of phytoplankton	k_c	0.64	$m^{-2}\ (mmol\ PO_4)^{-1}$

[a]Subscripts 1 and 2 refer to the large and small phytoplankton types, respectively.

Here ψ introduces the mentioned inhibition and κ_{IN} is the half-saturation constant of NO_3+NO_2.

Table A1 displays the values of the described parameters together with the most relevant ones involved in zooplankton and detritus equations. Plankton-size-independent parameters are the same as in *Follows et al.* [2007] and *Dutkiewicz et al.* [2009], whereas size-dependent parameters are in the range of small and large plankton given in these papers and elsewhere in the literature.

References

Arin, L., X. A. F. Morán, and M. Estrada (2002), Phytoplankton size distribution and growth rates in the Alboran Sea (SW Mediterranean): Short term variability related to mesoscale hydrodynamics, *J. Plankton Res.*, *24*(10), 1019–1033.

Brandt, P., W. Alpers, and J. O. Backhaus (1996), Study of the generation and propagation of internal waves in the Strait of Gibraltar using a numerical model and synthetic aperture radar images of the European ERS 1 satellite, *J. Geophys. Res.*, *101*(C6), 14,237–14,252.

Dutkiewicz, S., M. J. Follows, and J. G. Bragg (2009), Modeling the coupling of ocean ecology and biogeochemistry, *Global Biogeochem. Cycles*, *23*, GB4017, doi:10.1029/2008GB003405.

Echevarría, F., L. Zabala, A. Corzo, G. N. L. Prieto, and D. Macías (2009), Spatial distribution of autotrophic picoplankton in relation to physical forcings: The gulf of Cádiz, Strait of Gibraltar and Alborán Sea case study, *J. Plankton Res.*, *31*(11), 1339–1351.

Evans, M. A., S. MacIntyre, and G. W. Kling (2008), Internal wave effects on photosynthesis: Experiments, theory, and modeling, *Limnol. Oceanogr.*, *53*(1), 339–353.

Follows, M. J., S. Dutkiewicz, S. Grant, and S. W. Chisholm (2007), Emergent biogeography of microbial communities in a model ocean, *Science*, *315*(5820), 1843–1846, doi:10.1126/science.1138544.

García-Gorriz, E., and M.-E. Carr (1999), The climatological annual cycle of satellite-derived phytoplankton pigments in the Alboran Sea, *Geophys. Res. Lett.*, *26*(19), 2985–2988, doi:10.1029/1999GL900529.

García-Lafuente, J., E. Bruque, J. C. Sánchez-Garrido, G. Sannino, and S. Sammartino (2013), The interface mixing layer and the tidal dynamics at the eastern part of the Strait of Gibraltar, *J. Mar. Syst.*, *117–118*, 31–42, doi:10.1016/j.jmarsys.2013.02.014.

Geider, R. J., H. L. McIntyre, and T. M. Kana (1997), Dynamic model of phytoplankton growth and acclimation: Responses of the balanced growth rate and the chlorophyll a: Carbon ratio to light, nutrient-limitation and temperature, *Mar. Ecol. Prog. Ser.*, *148*, 187–200.

Griffies, S. M., and R. W. Hallberg (2000), Biharmonic friction with a Smagorinsky-like viscosity for use in large-scale eddy-permitting ocean models, *Mon. Weather Rev.*, *128*, 2935–2946.

Hammer, W. M., and I. R. Hauri (1981), Effects of island mass: Water flow and plankton pattern around a reef in the Great Barrier Reef lagoon, Australia, *Limnol. Oceanogr.*, *26*, 1084–1102.

Hasegawa, D., H. Yamazaki, R. G. Lueck, and L. Seuront (2004), How islands stir and fertilize the upper ocean, *Geophys. Res. Lett.*, *31*, L16303, doi:10.1029/2004GL020143.

Hernández-León, S. (1991), Accumulation of mesozooplankton in a wake area as a causative mechanism of the island-mass effect, *Mar. Biol.*, *109*(1), 141–147, doi:10.1007/BF01320241.

Holloway, G., and K. Denman (1989), Influence of internal waves on primary production, *J. Plankton Res.*, *11*(2), 409–413.

Huertas, I. E., A. F. Ríos, J. García-Lafuente, A. Makaoui, S. Rodríguez-Gálvez, A. Sánchez-Román, J. Orbi, J. Ruíz, and F. F. Pérez (2009), Anthropogenic and natural co_2 exchange through the Strait of Gibraltar, *Biogeosciences*, *6*(4), 647–662, doi:10.5194/bg-6-647-2009.

Hundsdorfer, W., and R. A. Trompert (1994), Method of lines and direct discretization: A comparison for linear advection, *Appl. Numer. Math.*, *13*(6), 469–490, doi:10.1016/0168-9274(94)90009-4.

Kalnay, E., et al. (1996), The NCEP/NCAR 40-year reanalysis project, *Bull. Am. Meteorol. Soc.*, *77*, 437–470.

La-Violette, P. E. (1984), The advection of submesoscale thermal features in the Alboran Sea Gyre, *J. Phys. Oceanogr.*, *14*, 550–565.

Lawrence, G. A. (1993), The hydraulics of steady two-layer flow over a fixed obstacle, *J. Fluid Mech.*, *254*, 605–633.

Lazzari, P., C. Solidoro, V. Ibello, S. Salon, A. Teruzzi, K. Béranger, S. Colella, and A. Crise (2012), Seasonal and inter-annual variability of plankton chlorophyll and primary production in the Mediterranean Sea: A modelling approach, *Biogeosciences*, *9*(1), 217–233, doi:10.5194/bgd-8-5379-2011.

Leichter, J. J., G. Shellenbarger, S. J. Genovese, and S. R. Wing (1998), Breaking internal waves on a Florida (USA) coral reef: A plankton pump at work?, *Mar. Ecol. Prog. Ser.*, *166*, 83–97.

Lohrenz, S. E., D. A. Wiesenburg, I. P. DePalma, K. S. Johnson, and D. E. Gustafson (1988), Interrelationships among primary production, chlorophyll, and environmental conditions in frontal regions of the western Mediterranean Sea, *Deep Sea Res., Part A*, *35*(5), 793–810, doi:10.1016/0198-0149(88)90031-3.

Long, R. R. (1954), Some aspects of the flow of stratified fluids: II. Experiments with a two-fluid system, *J. Fluid Mech.*, *6*, 97–115.

Losch, M., V. Strass, B. Cisewski, C. Klaas, and R. G. Bellerby (2014), Ocean state estimation from hydrography and velocity observations during EIFEX with a regional biogeochemical ocean circulation model, *J. Mar. Syst.*, *129*, 437–451, doi:10.1016/j.jmarsys.2013.09.003.

Macías, D., G. Navarro, F. Echevarría, C. M. García, and J. L. Cueto (2007a), Phytoplankton pigment distribution in the northwestern Alboran Sea and meteorological forcing: A remote sensing study, *J. Mar. Res.*, *65*(4), 523–543, doi:10.1357/002224007782689085.

Macías, D., A. Martin, J. Garciá-Lafuente, C. García, A. Yool, M. Bruno, A. Vázquez-Escobar, A. Izquierdo, D. Sein, and F. Echevarría (2007b), Analysis of mixing and biogeochemical effects induced by tides on the Atlantic-Mediterranean flow in the Strait of Gibraltar through a physical-biological coupled model, *Prog. Oceanogr.*, *74*(2–3), 252–272.

Maillard, C. (2002), MEDAR/MEDATLAS: A database for Mediterranean and Black Sea projects, *Rep. 16*, pp. 115–117, CIESM, IFREMER/SISMER, Cent. de Brest, Plouzane, France.

Marshall, J., C. Hill, L. Perelman, and A. Adcroft (1997a), Hydrostatic, quasi-hydrostatic, and nonhydrostatic ocean modeling, *J. Geophys. Res.*, *102*(C3), 5733–5752, doi:10.1029/96JC02776.

Marshall, J., A. Adcroft, C. Hill, L. Perelman, and C. Heisey (1997b), A finite-volume, incompressible Navier Stokes model for studies of the ocean on parallel computers, *J. Geophys. Res.*, *102*(C3), 5753–5766, doi:10.1029/96JC02775.

Mercado, J. M., T. Ramírez, D. Cortés, M. Sebastián, and M. Vargas-Yáñez (2005), Seasonal and inter-annual variability of the phytoplankton communities in an upwelling area of the Alboran Sea (SW Mediterranean Sea), *Sci. Mar.*, *69*(4), 451–465.

Morel, A., Y. Huot, B. Gentili, P. J. Werdell, S. B. Hooker, and B. A. Franz (2007), Examining the consistency of products derived from various ocean color sensors in open ocean (case 1) waters in the perspective of a multi-sensor approach, *Remote Sens. Environ.*, *111*, 69–88.

Muacho, S., J. da Silva, V. Brotas, and P. Oliveira (2013), Effect of internal waves on near-surface chlorophyll concentration and primary production in the Nazar canyon (west of the Iberian peninsula), *Deep Sea Res., Part I*, *81*, 89–96.

Nagai, T., A. Tandon, N. Gruber, and J. C. McWilliams (2008), Biological and physical impacts of ageostrophic frontal circulations driven by confluent flow and vertical mixing, *Dyn. Atmos. Oceans*, *45*(3–4), 229–251.

Navarro, G., A. Vázquez, D. Macías, M. Bruno, and J. Ruíz (2011), Understanding the patterns of biological response to physical forcing in the Alboran Sea (western Mediterranean), *Geophys. Res. Lett.*, *38*, L23606, doi:10.1029/2011GL049708.

Oguz, T., D. Macías, J. García-Lafuente, A. Pascual, and J. Tintoré (2014), Fueling plankton production by a Meandering Frontal Jet: A case study for the Alboran Sea (Western Mediterranean), *PLoS ONE*, *9*(11), e111482, doi:10.1371/journal.pone.0111482.

Pacanowski, R. C., and S. G. H. Philander (1981), Parameterization of vertical mixing in numerical models of tropical oceans, *J. Phys. Oceanogr.*, *11*, 1443–1451.

Pan, X., G. Wong, F.-K. Shiah, and T.-Y. Ho (2012), Enhancement of biological productivity by internal waves: Observations in the summertime in the northern South China Sea, *J. Oceanogr.*, *68*(3), 427–437.

Ramírez, T., D. Cortés, J. Mercado, M. Vargas-Yáñez, M. Sebastián, and E. Liger (2005), Seasonal dynamics of inorganic nutrients and phytoplankton biomass in the NW Alboran Sea, *Estuarine Coastal Shelf Sci.*, *65*(4), 654–670.

Reul, A., V. Rodríguez, F. Jiménez-Gómez, J. Blanco, B. Bautista, T. Sarhan, F. Guerrero, J. Ruíz, and J. García-Lafuente (2005), Variability in the spatio-temporal distribution and size-structure of phytoplankton across an upwelling area in the NW-Alboran Sea (W-Mediterranean), *Cont. Shelf Res.*, *25*(5–6), 589–608, doi:10.1016/j.csr.2004.09.016.

Ruíz, J., and G. Navarro (2006), Upwelling spots and vertical velocities in the Gulf of Cadiz: An approach for their diagnose by combining temperature and ocean colour remote sensing, *Deep Sea Res., Part II*, *53*(11–13), 1282–1293.

Sammartino, S., J. G. Lafuente, J. Sánchez-Garrido, F. D. los Santos, E. A. Fanjul, C. Naranjo, M. Bruno, and C. Calero (2014), A numerical model analysis of the tidal flows in the bay of Algeciras, Strait of Gibraltar, *Cont. Shelf Res.*, *72*, 34–46.

Sánchez-Garrido, J. C., G. Sannino, L. Liberti, J. García Lafuente, and L. Pratt (2011), Numerical modeling of three-dimensional stratified tidal flow over Camarinal Sill, Strait of Gibraltar, *J. Geophys. Res.*, *116*, C12026, doi:10.1029/2011JC007093.

Sánchez-Garrido, J. C., J. García-Lafuente, E. Álvarez-Fanjul, M. García-Sotillo, and F. J. de los Santos (2013), What does cause the collapse of the Western Alboran Gyre? Results of an operational ocean model, *Prog. Ocenogr.*, *116*, 142–153, doi:10.1016/j.pocean.2013.07.002.

Sánchez-Garrido, J. C., J. G. Lafuente, S. Sammartino, C. Naranjo, F. J. de los Santos, and E. A. Fanjul (2014), Meteorologically-driven circulation and flushing times of the bay of Algeciras, Strait of Gibraltar, *Mar. Pollut. Bull.*, *80*(1–2), 97–106.

Sangrà, P., G. Basterretxea, J. L. Pelegrí, and J. Arístegui (2001), Chlorophyll increase due to internal waves in the shelf-break of Gran Canaria Island (Canary Islands), *Sci. Mar.*, *65*, 89–97.

Sannino, G., J. C. Sánchez Garrido, L. Liberti, and L. Pratt (2014), Exchange flow through the Strait of Gibraltar as simulated by a sigma-coordinate hydrostatic model and a z-coordinate non-hydrostatic model, in *The Mediterranean Sea: Temporal Variability and Spatial Patterns*, pp. 25–50, John Wiley, Hoboken, N. J., doi:10.1002/9781118847572.ch3.

Sarhan, T., J. García-Lafuente, M. Vargas, J. M. Vargas, and F. Plaza (2000), Upwelling mechanisms in the northwestern Alboran Sea, *J. Mar. Syst.*, *23*(4), 317–331, doi:10.1016/S0924-7963(99)00068-8.

Siokou-Frangou, I., U. Christaki, M. G. Mazzocchi, M. Montresor, M. Ribera d'Alcalá, D. Vaqué, and A. Zingone (2010), Plankton in the open Mediterranean Sea: A review, *Biogeosciences*, *7*(5), 1543–1586, doi:10.5194/bg-7-1543-2010.

Sotillo, M. G., S. Caillea, P. Lorente, B. Levier, R. Aznar, G. Reffray, A. Amo-Baladrón, J. Chanut, M. Benkiran, and E. Alvarez-Fanjul (2015), The MyOcean IBI ocean forecast and reanalysis systems: Operational products and roadmap to the future Copernicus service, *J. Oper. Oceanogr.*, *8*(1), 63–79.

Spall, M. A. (1995), Frontogenesis, subduction, and cross-front exchange at upper ocean fronts, *J. Geophys. Res.*, *100*(C2), 2543–2557.

Steinacher, M., et al. (2010), Projected 21st century decrease in marine productivity: A multi-model analysis, *Biogeosciences*, *7*(3), 979–1005, doi:10.5194/bg-7-979-2010.

Uitz, J., D. Stramski, B. Gentili, F. D'Ortenzio, and H. Claustre (2012), Estimates of phytoplankton class-specific and total primary production in the Mediterranean Sea from satellite ocean color observations, *Global Biogeochem. Cycles*, *26*, GB2024, doi:10.1029/2011GB004055.

Vargas-Yáñez, M., T. Sarhan, F. Plaza, J. Rubín, and M. C. García-Martínez (2002), The influence of tide-topography interaction on low-frequency heat and nutrient fluxes. Application to Cape Trafalgar, *Cont. Shelf Res.*, *22*(1), 115–139.

Vlasenko, V., J. C. Sánchez-Garrido, N. Stashchuk, J. García-Lafuente, and M. Losada (2009), Three-dimensional evolution of large-amplitude internal waves in the Strait of Gibraltar, *J. Phys. Oceanogr.*, *39*, 2230–2246.

Wesson, J. C., and M. C. Gregg (1994), Mixing at Camarinal Sill in the Strait of Gibraltar, *J. Geophys. Res.*, *99*(C5), 9847–9878, doi:10.1029/94JC00256.